International Journal of Geo-Information

MDPI

Article

RETRACTED: Identifying Asphalt Pavement Distress Using UAV LiDAR Point Cloud Data and Random Forest Classification

Zhiqiang Li [1], Chengqi Cheng [2,*], Mei-Po Kwan [3,4], Xiaochong Tong [5] and Shaohong Tian [1]

1 Institute of Remote Sensing and Geographic Information System, Peking University, Beijing 100871, China; lzq.gis@pku.edu.cn (Z.L.); shaohongtian@pku.edu.cn (S.T.)
2 College of Engineering, Peking University, Beijing 100871, China
3 Department of Geography and Geographic Information Science, University of Illinois at Urbana-Champaign, Urbana, IL 61801, USA; mpk654@gmail.com
4 Department of Human Geography and Spatial Planning, Utrecht University, 3584 CB Utrecht, The Netherlands
5 Zhengzhou Institute of Surveying and Mapping, Zhengzhou 450001, China; txchr@163.com
* Correspondence: ccq@pku.edu.cn; Tel.: +86-133-2113-8499

Received: 22 December 2018; Accepted: 13 January 2019; Published: 16 January 2019



Abstract: Asphalt pavement ages and incurs various distresses due to natural and human factors. Thus, it is crucial to rapidly and accurately extract different types of pavement distress to effectively monitor road health status. In this study, we explored the feasibility of pavement distress identification using low-altitude unmanned aerial vehicle light detection and ranging (UAV LiDAR) and random forest classification (RFC) for a section of an asphalt road that is located in the suburb of Shihezi City in Xinjiang Province of China. After a spectral and spatial feature analysis of pavement distress, a total of 48 multidimensional and multiscale features were extracted based on the strength of the point cloud elevations and reflection intensities. Subsequently, we extracted the pavement distresses from the multifeature dataset by utilizing the RFC method. The overall accuracy of the distress identification was 92.3%, and the kappa coefficient was 0.902. When compared with the maximum likelihood classification (MLC) and support vector machine (SVM), the RFC had a higher accuracy, which confirms its robustness and applicability to multisample and high-dimensional data classification. Furthermore, the method achieved an overall accuracy of 95.86% with a validation dataset. This result indicates the validity and stability of our method, which highway maintenance agencies can use to evaluate road health conditions and implement maintenance.

Keywords: UAV; LiDAR; asphalt pavement distresses; pavement health conditions; multiscale features; random forest classification

1. Introduction

Highways are a strategic resource in a country and they provide the basis of social development [1]. With the development of China's economy, highway construction has made great progress. By the end of 2017, China's total highway mileage was 4,773,500 km [2]. Many factors (such as temperature, moisture, weathering, and loads) [3–5] can adversely affect pavement structure and result in a variety of road distresses, which not only influence the normal use of highways, but also lead to large economic losses. Therefore, identifying pavement distress is of great significance for road condition monitoring, road maintenance, and road management [6,7].

Many evaluation indexes (such as the pavement condition index, pavement roughness index, riding quality index, and pavement structure strength index) have been used to measure pavement

This paper has been retracted.
A retraction notice was published on 11 September 2019 in *ISPRS International Journal of Geo-Information* **2019**, *8*, 402; doi:10.3390/ijgi8090402

RETRACTED

quality and usage status [8,9]. To obtain these indexes, it is imperative to adopt reliable approaches [10]. Traditional methods utilize measurements that are taken in situ along with visual examinations and interpretations [11]. These methods can collect detailed pavement surface condition data for various types of distress and provide accurate and valuable information. However, these methods have some disadvantages, such as being time consuming [7], expensive [12], labor-intensive [13], and subjective [14]. As an efficient means of earth observation, remote sensing can obtain the spectral and spatial information of various road materials to quickly assess the road conditions of large road networks and improve the efficiency of road condition investigations [15,16]. Therefore, recent studies [17–20] have demonstrated a growing interest in remote sensing applications for pavement monitoring and management.

There has been evidence that pavement of different aging stages exhibits distinct spectral characteristics in reflectance and emissivity [4,21,22]. Asphalt surfaces lose bitumen over time and through degradation, thus increasing their reflectance values. As a result, pavements of different aging stages can be identified based on the variations in their reflectance values [19,23]. Moreover, as asphalt pavement deteriorates, its ability to absorb solar radiation gradually weakens [24]. That is, the thermal radiation information will change based on the pavement conditions. Therefore, previous research has focused on obtaining the spectral data of target sections using multispectral or hyperspectral sensors and then evaluating pavement usage status by comparing and analyzing the spectral features of asphalt pavement at different ages [25]. For example, Mei et al. analyzed field and laboratory data with the goal of differentiating asphalted surfaces. Multispectral Infrared and Visible Imaging Spectrometer (MIVIS) airborne data and multispectral images, such as Quickbird and Ikonos, were used. The study adopted the Spectral Angle Mapper (SAM) classifier and obtained an overall accuracy of 95% for Ikonos, 98% for Quickbird and 93% for MIVIS [23]. Pan et al. presented an experimental study of mapping road pavement conditions from the WorldView-2 based on endmember spectral mixture analysis. The analysis of the in situ measured spectra of asphalt road pavement showed that asphalt pavements in different aging conditions exhibit quite different spectral patterns over the range of 0.35 to 2.5 μm. The assessment of the analysis results showed that the method is capable of classifying road pavements with an overall accuracy of 81.71% and Kappa coefficient of 0.77, when the in situ data were used as a reference [25]. However, there are many disadvantages to identifying asphalt pavement distress using remotely sensed imagery, such as the high cost of data acquisition, the long data acquisition cycles, and the use of remote sensors that are not sufficiently flexible. In addition, because of the spectral similarity among different types of pavement distress, it is difficult to obtain accurate results by only relying on spectral features [25,26].

In fact, nearly all of the current pavement condition assessment indexes require elevation information. As an efficient spatial data acquisition method, light detection and ranging (LiDAR) can provide the three-dimensional spatial information for a road section in a convenient, flexible, and rapid manner to obtain key information (such as rutting, pothole depths, and road surface roughness) that is needed to evaluate pavement conditions [27]. Many efforts have contributed to the extraction and monitoring of pavement distress by using LiDAR point cloud data [28–30]. Among them, [28] demonstrated the feasibility of using a three-dimensional (3D) laser-based pavement data acquisition system to conduct automated pavement cracking surveys. The experimental tests were conducted on actual pavements in Georgia. Based on the experimental results, the 3D laser pavement data are robust under different lighting conditions and low-intensity contrast conditions and they have the capability to address different contaminants on a pavement's surface. [29] introduced a real-time 3D scanning system for pavement distortion inspections. The system used the simple but robust structured light method for 3D profile generation. Pavement distortion distress, such as rutting and shoving, can be reliably detected from 3D transverse profiles, and the real-time measurements and 3D visualization of these distortions can be output to a pavement management system. [30] explored how LiDAR can be applied to identify and quantify the severity and coverage of pavement distress to calculate the required amounts of filling materials. However, vehicle-mounted LiDAR often affects normal traffic

RETRACTED

and incurs high monetary and resource costs. For long road sections, only a sample survey method can be adopted. In addition, it is difficult to ensure that the sampling is comprehensive for multilane pavement. Therefore, vehicle-mounted LiDAR cannot quickly, effectively, or regularly obtain the pavement health conditions of an entire road section.

With the rapid development of unmanned aerial vehicle (UAV) technology, UAV-based remote sensing has matured and has been widely used in agricultural, geological, and environmental monitoring [31]. UAV is a flexible platform that can be configured with various remote sensing sensors, in which digital images are the most commonly used data type. Several methods [25,26,32–35] that are based on digital image processing and machine learning algorithms have been proposed for pavement distress detection, using high-resolution images that were acquired from UAV platforms. For example, Kim utilized a simple UAV system to capture the pavement images and detected cracks based on the image binarization method [32]. Georgopoulos extracted the flexible pavement cracks using the digital image processing tools [36]. However, some limited abilities and issues occurred in these studies. For instance, some of the undamaged regions (such as tire tracks, oil stains, and traffic lines) intersecting with pavement damage prevent the detection of damages in the images because the collected images do not have any depth information. Moreover, macroscopic monitoring of pavement based on image processing methods always requires too many images. In comparison of two sequential images, the pixel values at the same location have a bias because of the illumination differences that are caused by the different solar incident angles. Consequently, this will lead to some degree of difference between the segmentation results of the same target derived from different images [25]. When compared with digital images, LiDAR can directly acquire the 3D spatial information of the deteriorated pavement to measure the geometric dimensions of the pavement distress and can more easily monitor the entire pavement. Furthermore, LiDAR is not restricted by the sun angle and can be implemented during the day and night [7]. Enlightened by these characteristics of LiDAR, the pavement point cloud data were captured and first attempted to identify the pavement distress in our study. The objective of this study is to develop a pavement distress identification approach for the asphalt pavement using LiDAR point cloud data (Figure 1). Specifically, an optimized feature set will be studied and a random forest classifier will be implemented and compared with other classification methods to demonstrate the robustness of the RFC in pavement distress classification.

RETRACTED

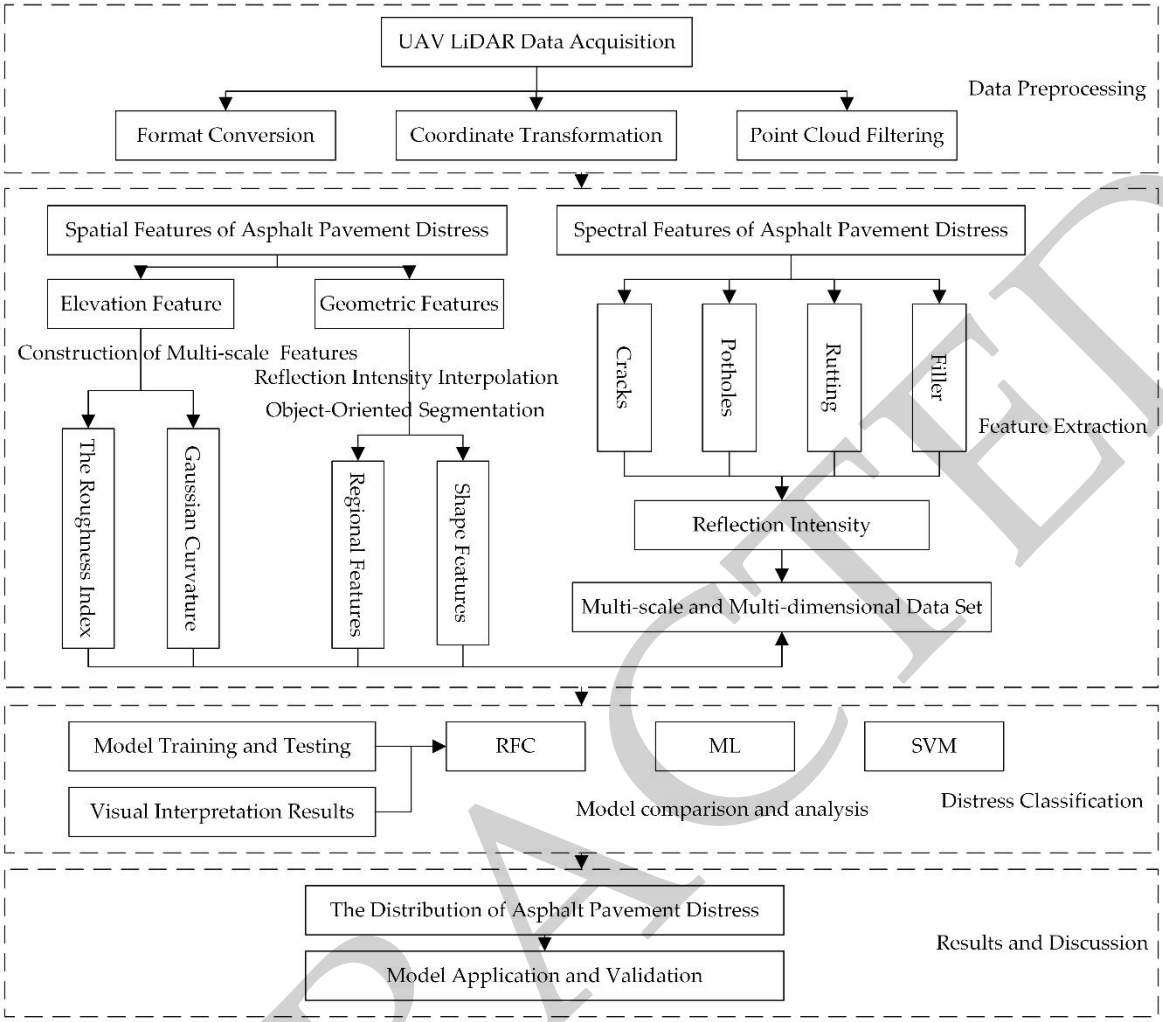


Figure 1. Research roadmap.

2. Data Acquisition and Preprocessing

2.1. Study Area

The road section that is selected for this study is a section of an asphalt road in the northern suburb of Shihezi City in Xinjiang Province of China (Figure 2). The pavement has been severely damaged, and roadbed materials are exposed in some areas and filled with gravel, loess, and grit. There are several longitudinal cracks and potholes along the moving directions of vehicles. Because of the unique meteorological, hydrological, and geological characteristics of Shihezi, the subgrade is not sufficiently stable. A certain degree of distortion appears along the road, and road attachments, such as curbstone and road signs, are seriously damaged. The areal extent of the pavement distress is fairly large, which makes it very suitable for data acquisition and analysis using low-altitude UAV and low-density point cloud data. The area is of great value for the development of an asphalt pavement distress extraction method that is based on low-altitude UAV LiDAR and the assessment of this method's feasibility.

RETRACTED



Figure 2. Study Area.

2.2. LiDAR Data Acquisition

We conducted our research using a B1-100 UAV manufactured by Scout and a RIEGL VUX-1LR laser scanner (Figure 3). The UAV platform was equipped with an INS/GPS flight control system, with up to 31 kg of payload and two hours of flight endurance. The RIEGL VUX-1LR is a lightweight and compact airborne laser scanner with an accuracy of 15 mm (http://www.riegl.com/nc/products/airborne-scanning/produktdetail/product/scanner/49/). The sensor enables high-speed data acquisition through a near-infrared laser beam and fast line scanning, which results in high-quality measurements even under poor atmospheric conditions.



Figure 3. Light detection and ranging (LiDAR) data acquisition system.

We gathered the point cloud data of the asphalt pavement near Dayushu Village in the northern suburb of Shihezi City on June 23, 2017. It was a sunny and windless day, which was very suitable for UAV system operation and flight. During this experiment, the UAV's flight altitude was 30 m, the view angle of the laser scanner was 55°, the flight speed was 5 m/s, and the original point cloud data included approximately 70,000,000 points. The point density of the LiDAR point cloud data was 40/m^2. However, the data cannot be directly used for pavement modeling because the original point cloud data adopted a geocentric coordinate system and it included too much noise. Therefore, the original data needed to be preprocessed before pavement distress could be extracted.

REJECTED

2.3. Point Cloud Data Preprocessing

2.3.1. Generating Standard Point Cloud Data

We used the postprocessing software RT Post-Process to convert the point cloud to an LAS format, which is an industry-standard binary format for storing airborne LiDAR data. The original point cloud data included the data that were acquired using the laser scanner, the flight path position, and the altitude data that were recorded by the IMU/GPS (Inertial measurement unit/GPS). The data preprocessing was divided into two steps. First, the IMU/GPS flight trajectory data were calculated and clipped. Subsequently, the original point cloud was segmented by using the clipped trajectory data.

The point cloud data that were selected for the experiment were between 346 s and 376 s, with a total length of approximately 150 m. As shown in Figure 4, the UAV flight direction was relatively stable during this time period (indicated by the double arrow). As mentioned in Section 2.2, the UAV's flight altitude was set to 30 m during the flight. The format of the clipped point cloud data was set as LAS and the coordinate system was set as WGS84.

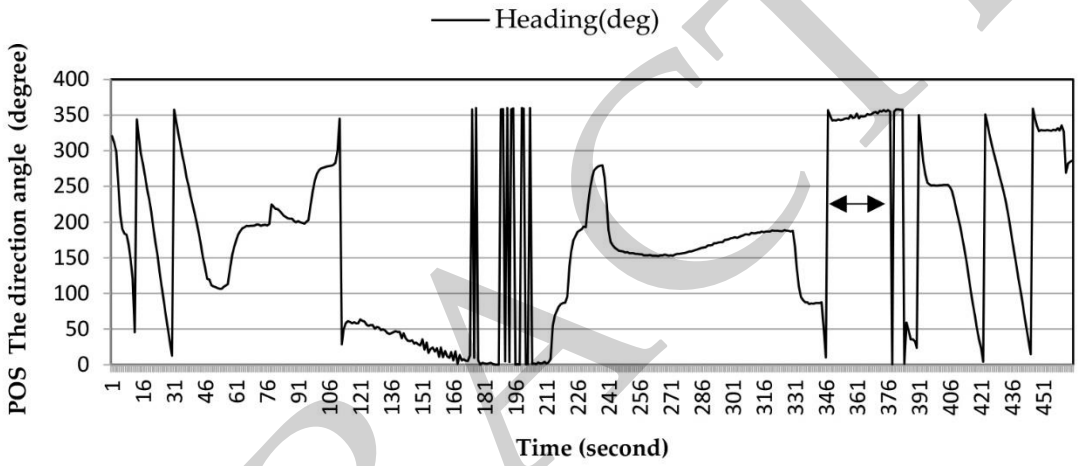


Figure 4. Direction angle variation in the POS system of an unmanned aerial vehicle (UAV) flight.

2.3.2. Point Cloud Filtering

During the data acquisition process, laser pulses could penetrate the leaves of vegetation or the glass of vehicles to form multiple reflection echoes. Therefore, it was necessary to conduct point cloud filtering to restore the reasonable distribution of the point cloud in space.

The point cloud filtering process was divided into three steps to eliminate outliers, noise, and redundant data. First, we utilized the classification tool of the RT Post-Process software to collect outliers from the point cloud visualization, and we removed them from the standard point cloud data. Most of these outliers resulted from the reflection and scattering of air dust on the laser and the reflection effect of water bodies on the laser. Therefore, their elevation values were lower or higher than elevations of their neighborhoods. Subsequently, it was necessary to filter the noise near vegetation and vehicles that formed because of multiple reflections. Here, we adopted a statistically based point cloud filtering algorithm to eliminate the noise points [37]. The algorithm assumes that the data are generated by a stochastic process, and typically, a closed-form probability distribution is fit to the data. Any data instance that is unlikely to be generated from the estimated stochastic process is then reported as noise [37]. Finally, there was a large amount of redundant data that needed to be eliminated from both sides of the road, including that of cultivated land, crops, and vegetation. The redundant data could be removed by elevation and scanning angle filtration. According to the measured data, the elevation of the selected road section was between 340 m and 343 m. Moreover, the scanning angle

RETRACTED

range was calculated at approximately 25°. Therefore, the filtering parameters of elevation (Ali) and scanning angle (θ) were as follows:

$$339.5 < Ali < 343.5 \quad (1)$$

$$-25 < \theta < 25. \quad (2)$$

After the completion of point cloud filtering, the point cloud data could be used for feature extraction and classification (Figure 5).

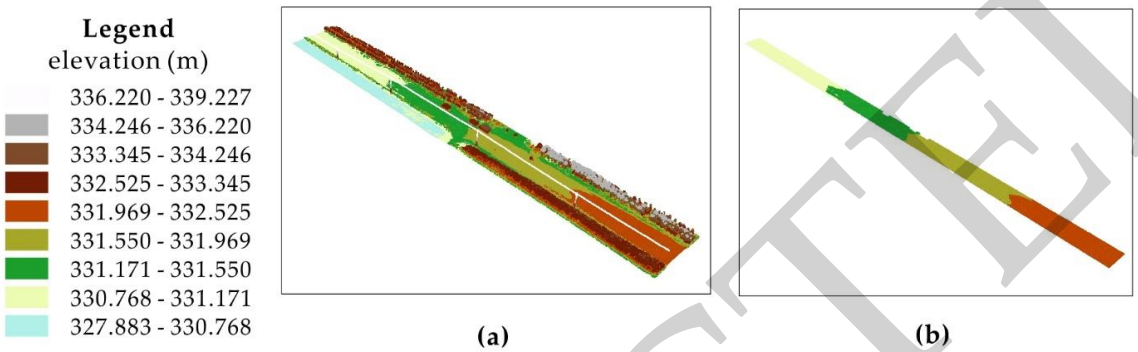


Figure 5. Point cloud filtering. **(a)** The original point cloud; and, **(b)** the pavement point cloud.

We obtained the pavement point cloud for a length of approximately 150 m. To verify the effectiveness and stability of our method, the point cloud was divided into two parts: experimental data and validation data. The experimental data were approximately 90 m, including approximately 900,000 laser pulse points, and this road section was more seriously damaged. The validation data were approximately 45 m, including approximately 400,000 laser pulse points, and they were used to validate the applicability and stability of the method for different road sections with various conditions.

3. Multi-Dimensional and Multi-Scale Feature Extraction

3.1. Elevation Feature

Many factors (including the volatilization of light components, light aging, temperature changes, humidity changes, and vehicle load) can result in asphalt pavement aging and they can cause a variety of pavement distress, such as cracks, potholes, subsidence, and rutting [38]. Different types of asphalt pavement distress have an obvious difference in elevation. Here, we provide a qualitative analysis based on the triangulated irregular network (TIN) model of the selected road to elaborate the elevation difference of various types of pavement distress. As Figure 6 shows, there are several cracks and potholes in the road section. The elevation of cracks and potholes is lower than that of undamaged pavement, while the elevation variation in subsidence areas is less than that in potholes. This difference is because asphalt mixtures on the subgrade are worn away in potholes, and the roadbed is exposed. Although subsidence is also obvious, the asphalt mixture layer is not completely lost. Potholes are often filled with other materials and, thus, do not show the typical spectral features that are different from undamaged pavement. However, the spatial features (circular or oval-shaped) of potholes are unique and obvious. Therefore, the elevation feature is of great importance for the subsequent pavement distress classification.

RETRACTED

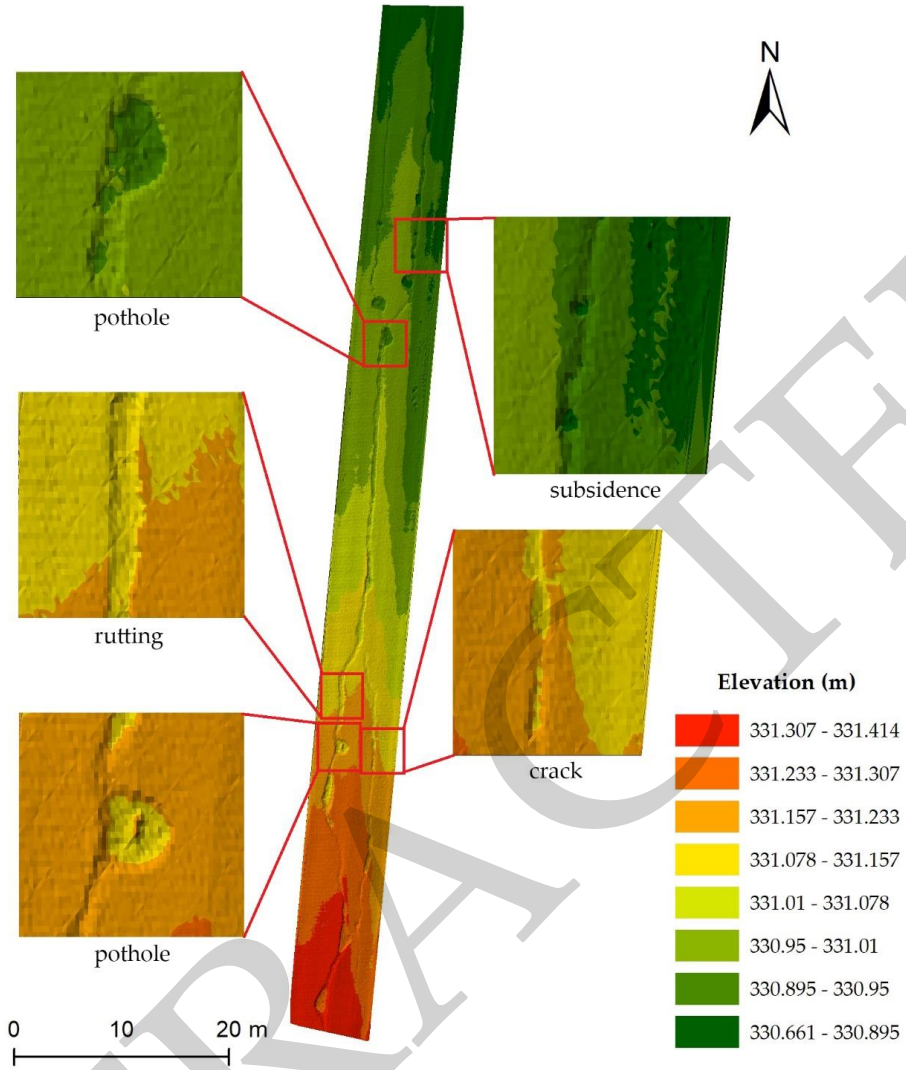


Figure 6. Triangulated irregular network (TIN) model of the road section in the study area.

3.2. Multi-Scale Statistical Features of Elevation

Pavement distresses are often isolated point groups or singular points at a certain measurement scale. It is necessary to establish a microscale model near these points to effectively extract features. For different types of pavement distress, the optimal measurement scale that is required for feature extraction is different. As a result, to obtain comprehensive and accurate features of pavement distress, we need to extract and analyze the features of pavement distress at multiple scales. To construct multiscale pavement point cloud features, we need to construct a hierarchy structure on the pavement point cloud data to achieve the transfer of feature information between different scales. The most commonly used method is to convert point cloud data into high-resolution images and to construct multiscale image features using a pixel-based scale transformation method. The pixel-based scale transformation approach is simple and easy to use. However, it cannot effectively utilize the spatial neighborhood information that is contained in the original point cloud. Therefore, we extracted the multiscale statistical features directly from the different neighborhood scales using the original point cloud rather than an intermedium, which avoids the loss of information.

To define reasonable measurement scales, we collected the geometric parameters of several types of typical pavement distress in the selected road (Table 1). By measuring the geometric parameters, we found that the geometric parameters of the potholes and subsidence were excessively large and that the average geometric scale was 50 cm. Although the width of some longitudinal cracks and

RETRACTED

transverse cracks is approximately 1~3 cm, these cracks cannot be expressed in the low-density point cloud data because the minimum interval of the data is approximately 5 cm. When considering the limitation in data quality, slight distress is not a priority in this study. In the vertical direction, the elevational precision was between 5 mm and 10 mm; thus, the elevational variation in severe types of distress, such as potholes, can be extracted. Therefore, to extract multiscale statistical features that are more consistent with the target pavement, the multiscale parameters were set as reported in Table 2.

Table 1. Geometric parameters of several types of typical pavement distress in the selected road.

Types of Distress	Length/Width/Depth	Grade	Thumbnail Photo
Pothole	6 m/30 cm/5 cm	Depth > 15 mm; Severe	
Pothole	3 m/117 cm/10 cm	Depth > 15 mm; Severe	
Pothole	2.4 m/111 cm/7 cm	Depth > 15 mm; Severe	
Subsidence (rutting)	5.5 m/19 cm/3 cm	Depth > 15 mm; Severe	
Longitudinal Crack	6~8 m/1~2 cm/--	Width $\leq$ 5 cm; Slight	
Longitudinal Crack	--/0.4~2 cm/--	Width $\leq$ 5 cm; Slight	
Transverse Crack	--/0.3~1.2 cm/--	Width $\leq$ 5 cm; Slight	
Transverse Crack	--/1~3 cm/--	Width $\leq$ 5 cm; Slight	

Table 2. Different measurement scales.

Type	Minimum Scale	Maximum Scale	Step Length	Number of Features
Microscopic Scale	20 cm	100 cm	5 cm	16
Macroscopic Scale	100 cm	200 cm	50 cm	3

RETRACTED

We can extract various microscopic features near a pavement distress at a microscopic scale and express the variation trend in the entire pavement at a macroscopic scale. According to the aforementioned ideas, a multiscale roughness index and Gaussian curvature were calculated.

(1) Roughness index

The roughness index is widely used in feature extraction using a LiDAR point cloud [39,40]. The traditional roughness index is defined as the ratio of the digital surface model (DSM) surface area to the digital elevation model (DEM) surface area. However, this definition is subject to quadratic accuracy loss during the process of generating DSM/DEM and calculating the surface area of DSM/DEM. To reduce the accuracy loss, we adopted the following definition: the roughness index of a point is equal to the distance between the point and a plane, which is the optimal fitting plane of the point and its neighboring points in a particular neighborhood (Figure 7). The error constraint of the optimal fitting plane is based on the least squares estimation method. The expression of the roughness index is as follows:

$$Roughness_i = \text{distance}\left((x_i, y_i, z_i), Z_{scale_j} = a_0 \cdot x + b_0 \cdot y + c_0\right) \quad (3)$$

where (x_i, y_i, z_i) is the spatial coordinate of the i^{th} laser pulse point and Z_{scale_j} is the optimal fitting plane of the i^{th} laser pulse point and its surrounding points at the j^{th} scale.

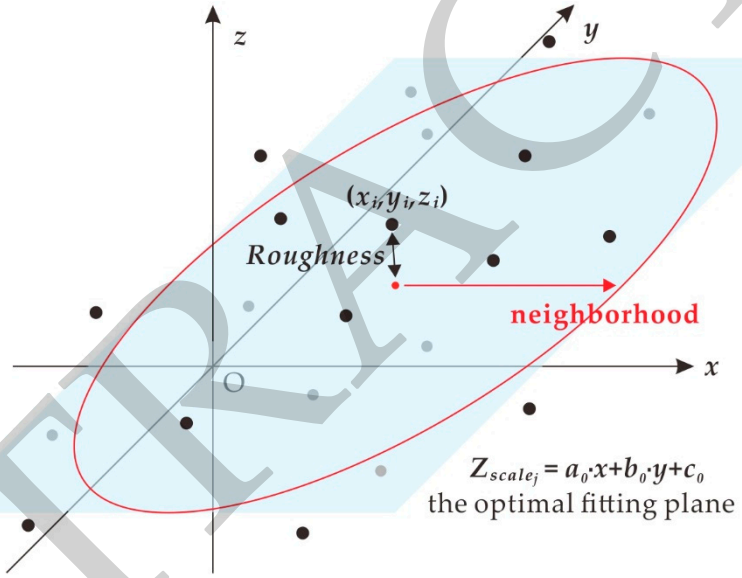


Figure 7. Definition of roughness.

As shown in Figure 8, the microstructure of pavement distress is well expressed at the microscopic scales. As the elevation varies, the roughness index at the edge of a pavement distress is much greater than that in other regions. At a small measurement scale, the asphalt mixture in the middle of potholes is completely lost, and the roughness index is relatively low due to the absence of filler. At a large measurement scale, although the middle of potholes is relatively flat, the roughness index is still high, and the features of pavement distress are expressed. At several large measurement scales (Figure 9), some undamaged pavement areas also have higher roughness indexes because of their closeness to seriously damaged regions, which indicates the sensitivity of the roughness index to the neighborhood statistics and it is also an early warning for the risk of pavement distress. While considering that the optimal measurement scale that is required for feature extraction is different for various types of distress, the construction of multiscale roughness indexes is a promising approach to comprehensively and accurately represent the features of pavement distress.

RETRACTED

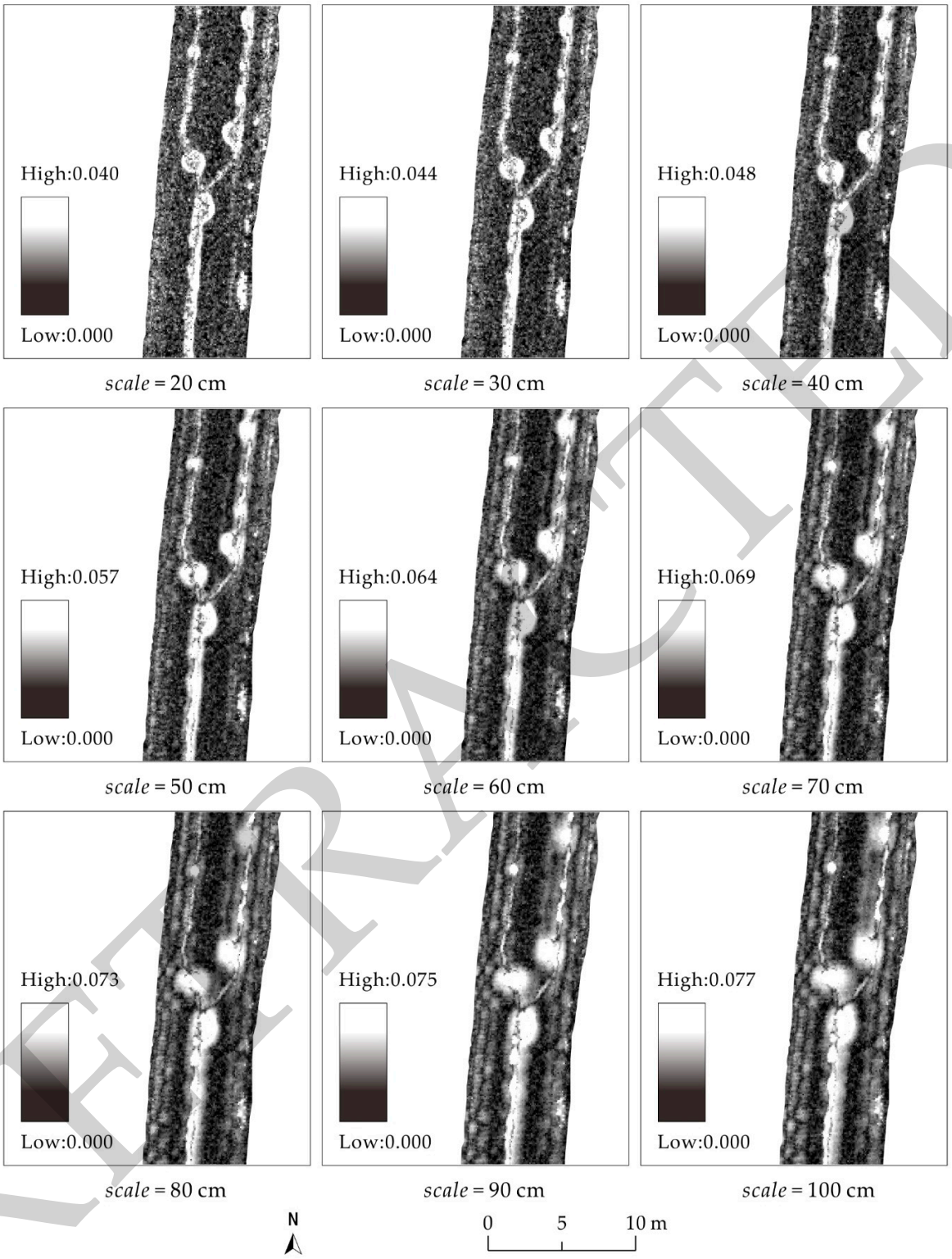


Figure 8. Distribution of the roughness index on microscopic scales.

RETRACTED

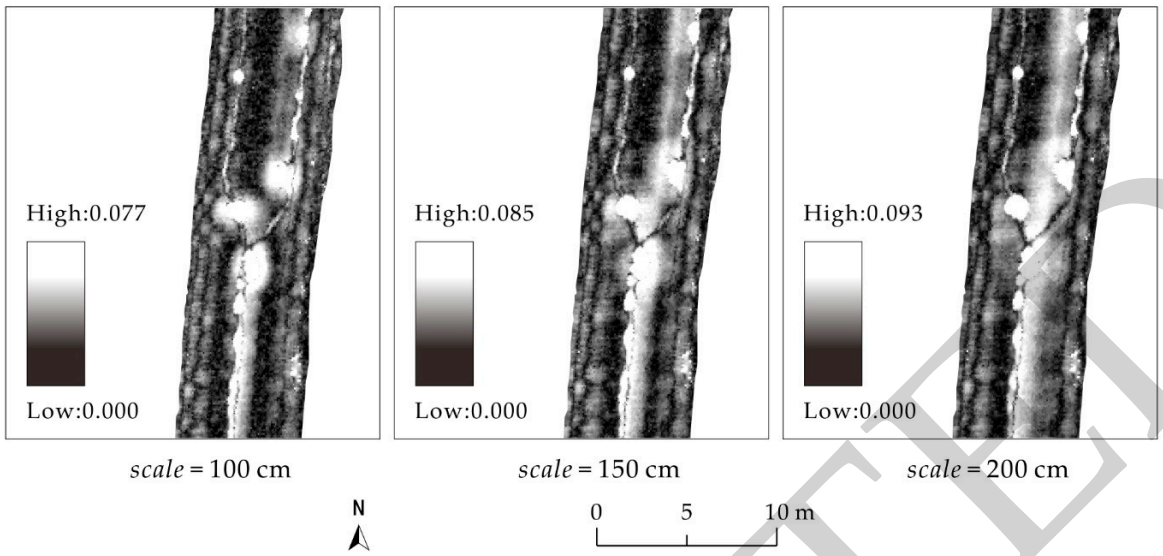


Figure 9. Distribution of the roughness index on macroscopic scales.

(2) Gaussian curvature

The occurrence of pavement distress is a process of the gradual erosion of undamaged pavement. The elevational variation in pavement reflects the characteristics of the gradient at a certain measurement scale. Therefore, we adopted Gaussian curvature to extract pavement distress. According to Gauss's Theorema Egregium [41], the Gaussian curvature is independent of its embedding position in space. Therefore, the use of Gaussian curvature can avoid the influence of the spatial position variation in fitting the quadratic surface in the curvature calculation when the measurement scale changes.

As shown in Figure 10, the asphalt mixture in the subsidence distress is not completely lost. The surface of these regions is very near a spherical or cylindrical surface, which has an effective expression on the distribution diagram of the Gaussian curvature at microscopic scales. The middle area of the potholes is relatively even and it shows the characteristics of a plane; thus, the Gaussian curvature is very small and it is similar to the roughness index. However, unlike the roughness index, which is easily influenced by neighborhood elevation at the macroscopic scale, the Gaussian curvature can be used to extract the distribution of pothole distress at a large measurement scale (Figure 11), even when the distress is serious or the area is large. At a large measurement scale, potholes with heavier damage can be effectively extracted. Meanwhile, adjacent undamaged pavement does not exhibit a large curvature. Therefore, by constructing and analyzing the multiscale Gaussian curvature of pavement in three-dimensional space, different types of distress can be effectively extracted.

RETRACTED

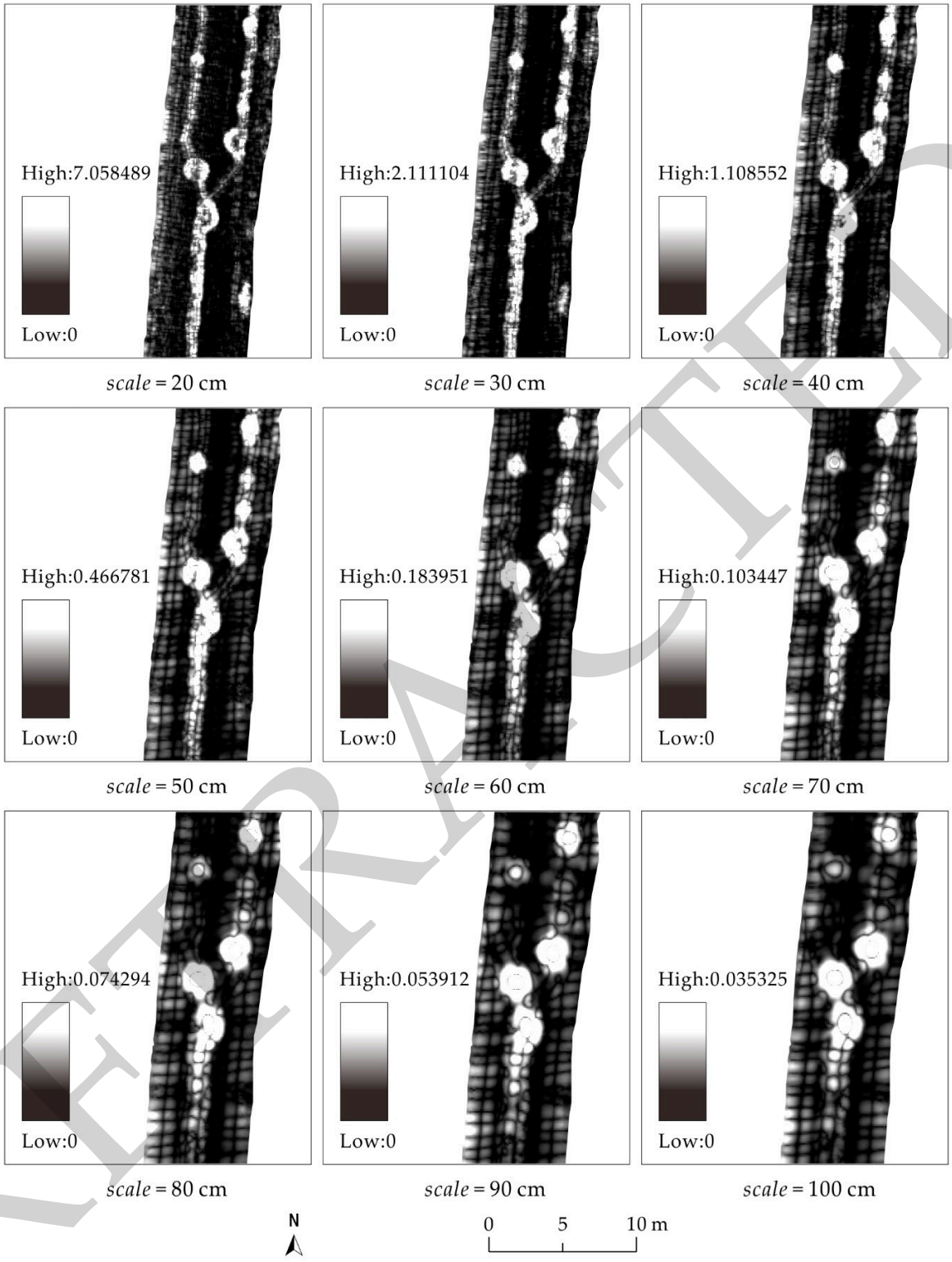


Figure 10. Distribution of Gaussian curvature on microscopic scales.

RETRACTED

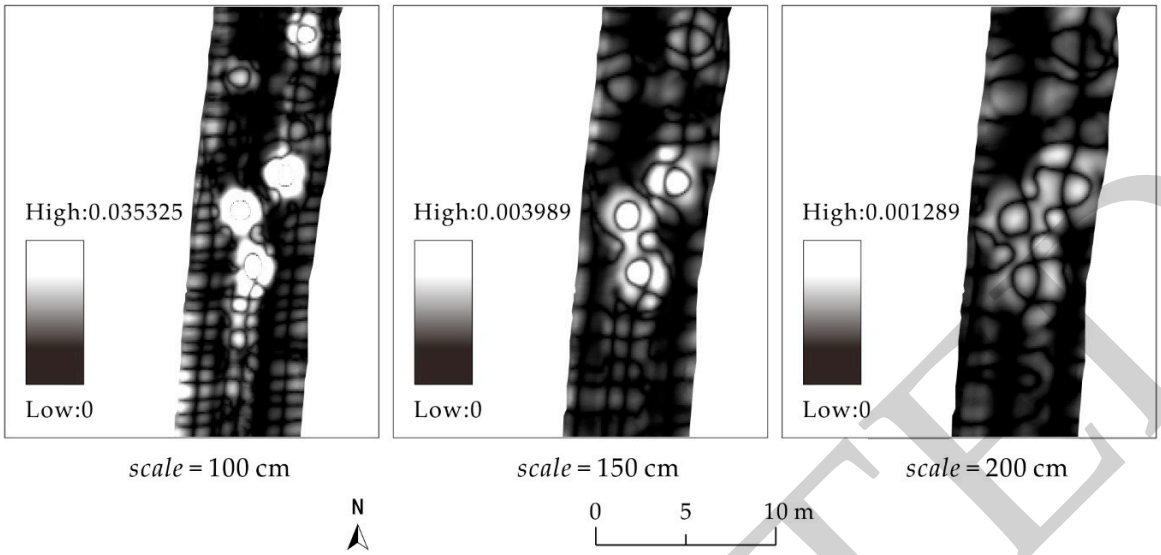


Figure 11. Distribution of Gaussian curvature on macroscopic scales.

3.3. Reflection Intensity Feature

Reflection intensity has a linear relationship with spectral reflectivity. We can construct a reflection intensity image with the reflection intensity attribute of the point cloud. Thus, different types of pavement distress can be extracted based on their reflection intensity feature. In this study, the elevational variation in the selected road section is quite small and it shows a continuous surface at the macroscopic scale and a cliff feature at the microscopic scale. Therefore, we adopted the inverse distance weighted method, which is frequently used and it is known to be stable in point cloud interpolation [42]. The interpolated image has a pixel size of 5 cm, as shown in Figure 12.

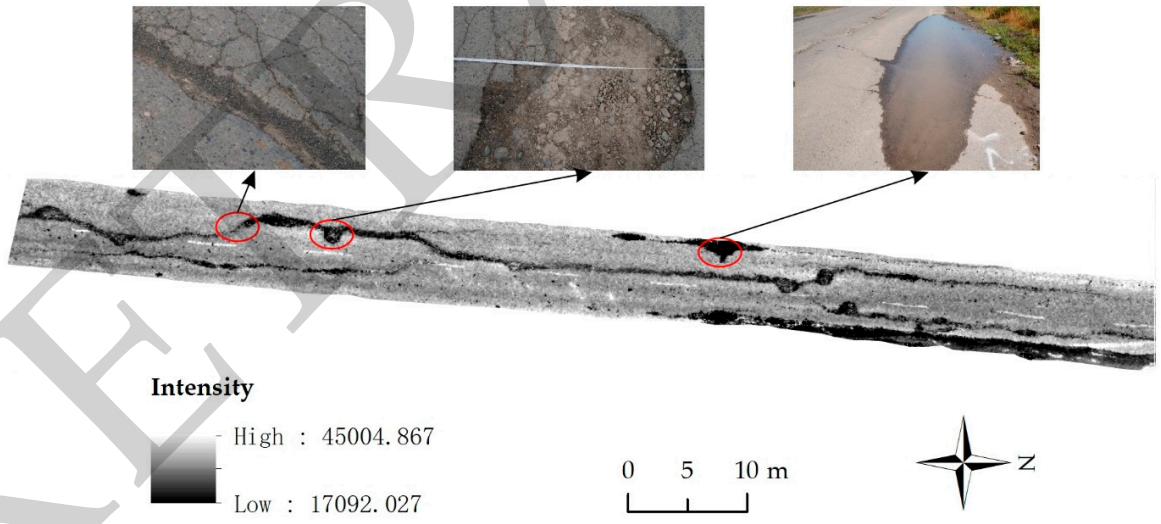


Figure 12. Reflection intensity interpolated image.

Figure 12 shows that pavement distresses in the selected road are very serious. There are many circular potholes and several longitudinal cracks along the road. There are some regions with low reflection intensity on both sides of the road, which result from the decrease in the reflection intensity in the near-infrared band due to the absorption of rainwater. Because of rainwater filling, the reflection intensity and elevation are affected by the absorption of laser energy and the refraction of water, which cause some errors in distress extraction.

RETRACTED

3.4. Object-Oriented Geometric Features

The reflection intensity image reflects spectral features in the midinfrared band. In addition to the obvious difference with undamaged pavement in the spectrum, pavement distresses also have unique geometric features that can be calculated to compensate for the deficiency in the spectral information. Here, object-oriented segmentation of the reflection intensity image was performed to extract the geometric features of the pavement distress. We adopted the intensity segmentation algorithm that was provided by ENVI/IDL, which is based on pixel brightness and is best for segmenting images with subtle gradients. By adjusting the scale threshold of the segmentation and merging, a good segmentation result was obtained when the parameters of the segmentation scale and merging scale were set to 10 and 15, respectively. The segmentation results are presented in Figure 13. The segmentation result indicates that areas with severe distress are basically divided into a complete region, while areas with better pavement conditions are divided into many small patches because of the aging of undamaged pavement.

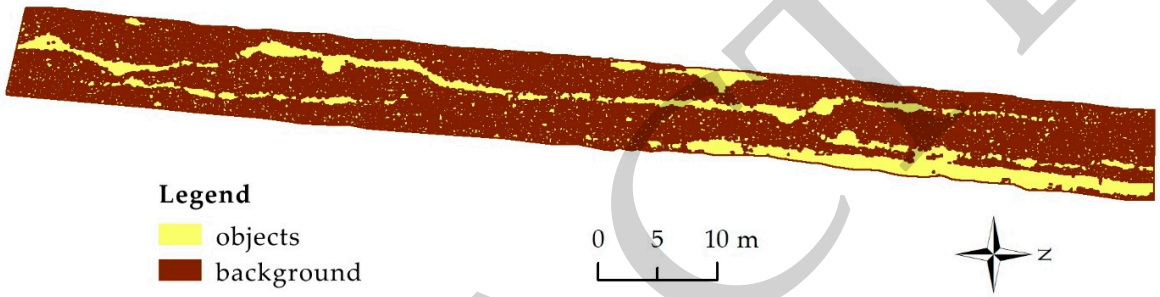


Figure 13. Object-oriented segmentation results.

We extracted the geometric features of the segmentation results using the Feature Extraction module provided by ENVI/IDL, including the regional features and shape features. The regional features included the area, perimeter, extensibility, and main direction, which were used to describe the regional attributes. These attributes were influenced by the segmentation parameters, but the features of different types of objects could be expressed in a satisfactory segmentation result. The shape features included the shape factor, compactness, circularity, and rectangularity. These features were primarily used to evaluate the specific geometrical morphology of an object's boundary. Some types of distress often have significant changes in the regional features but they have a relatively stable distribution in the contours, which increases the accuracy of the distress extraction.

Figure 14 shows the distribution of four regional features. According to the segmentation result, the polygonal patches in the damaged areas are relatively large. Correspondingly, the area and perimeter features are also large. Most of the pavement distress is distributed along the north-south direction; thus, their extensibility is generally higher than that of undamaged pavement. The main direction reflects the principal direction of the deformed objects. In undamaged pavement, the main direction is randomly distributed because of the fragmentized segmentation result, while the main direction in the damaged regions is consistent.

RETRACTED

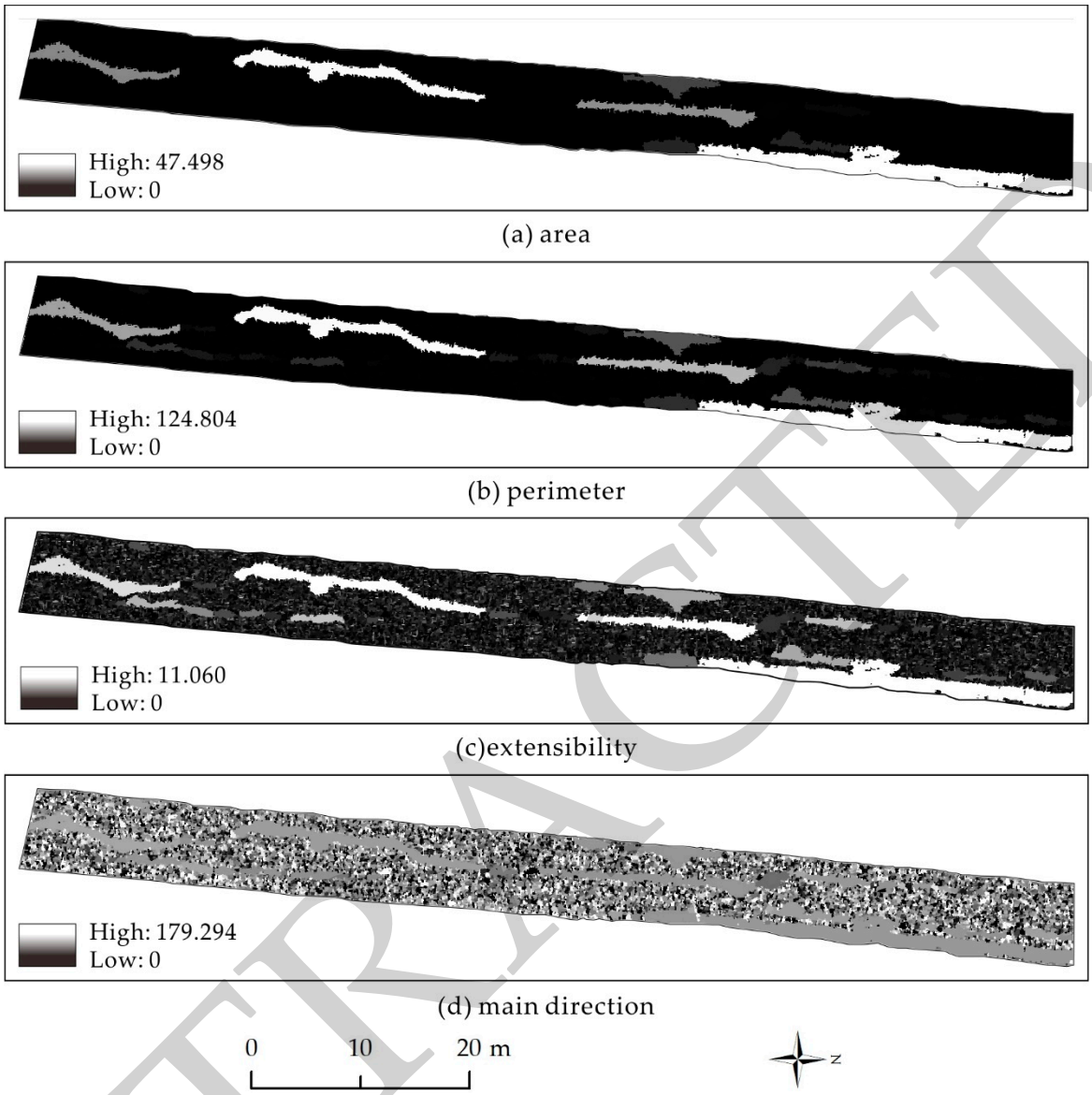


Figure 14. Regional features of objects after segmentation.

Shape factors are dimensionless quantities that are used in image analysis and numerically describe the shape of a polygon, independent of its size. The dimensionless quantities are utilized to represent the degree of deviation from a circle. Compactness is adopted to measure the degree of tightness for a polygonal boundary and the circle is the best compact shape. Circularity is used to measure the circular feature of a polygon, where the value of a standard circle is 1. Similarly, rectangularity is a measure of the rectangular feature, where the value of a rectangle is 1. These four features are calculated to measure the shape of the polygons (Figure 15). Some typical distresses, such as potholes, subsidence, and upheaval, have very recognizable geometrical shapes. The calculations of these shape features play an important role in pavement distress extraction and different types of distress distinctions.

RETRACTED

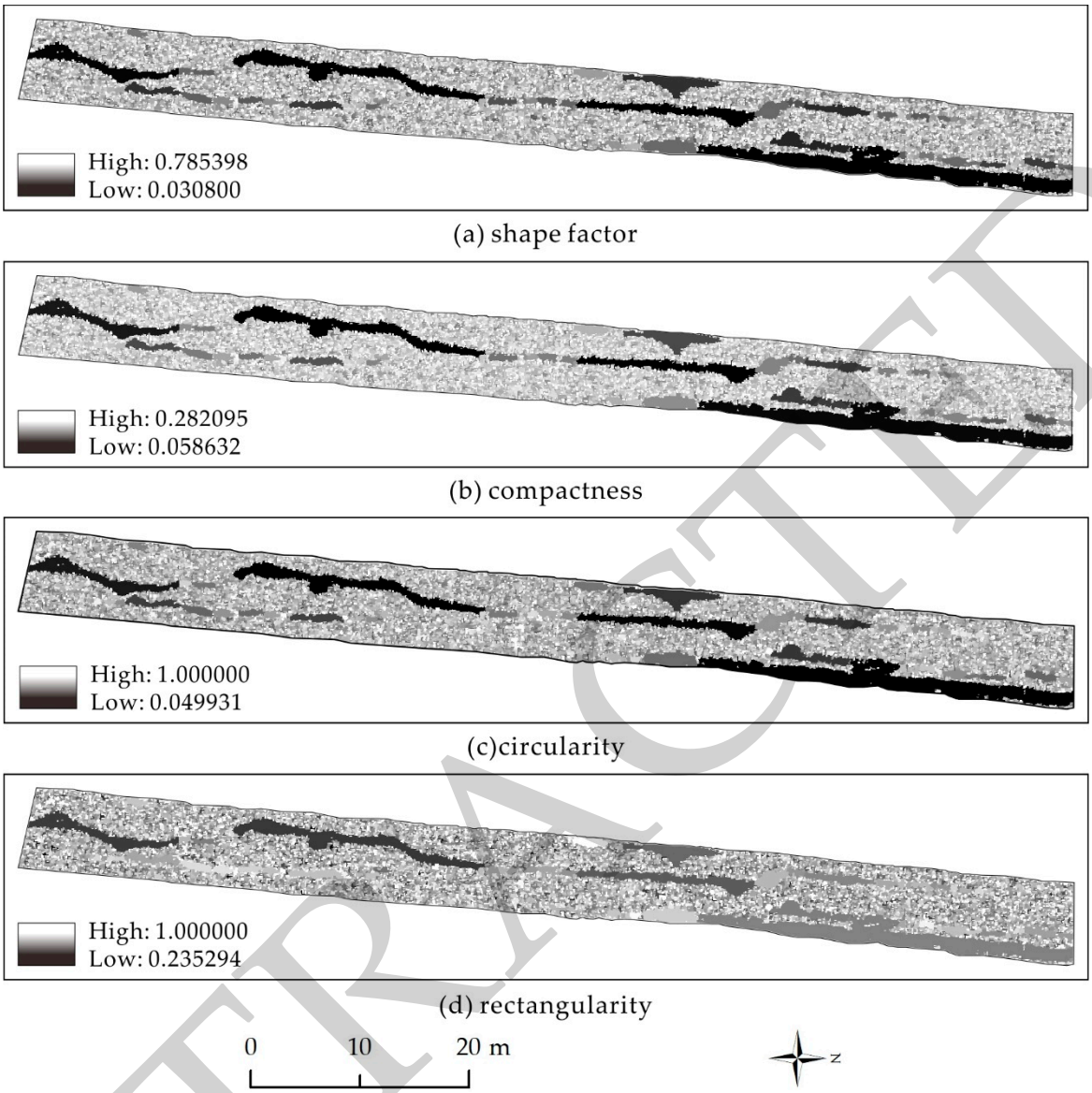


Figure 15. Shape features of objects after segmentation.

4. Asphalt Pavement Distress Classification Using Random Forest

4.1. Principles of Random Forest Classification

In this study, we extracted a total of 48 features for pavement distress classification, including an elevation feature, multiscale statistical features, a reflection intensity feature, and object-oriented geometric features. Since these features have a certain degree of correlation, traditional classification methods that are based on probability and statistics have difficulties in such a situation. Therefore, RFC, which has a strong ability to reduce the correlation between the trees and the generalization error [43], was used. RFC has high classification accuracy and robustness and it has excellent applicability to multisample and high-dimensional data classification [44].

RFC is an ensemble classification that refers to a new approach that uses not just one, but rather many decision trees. Each decision tree is generated according to the training set and a random vector, θ_k, in which the random vectors that are used to generate each decision tree are independently identically distributed. The final decision tree set is the RFC model $\{h(X, \theta_k), k = 1,2, \ldots, K\}$, where X is an input vector [45]. Each single decision tree $h(X, \theta_k)$ has a vote to select the classification result of input vector X. After K-round training, a classification model sequence $\{h_1(X), h_2(X), \ldots, h_K(X)\}$ can

RETRACTED

be obtained according to the training set, and the RFC model is developed. The classification result of the sample set is determined by a simple vote, as follows:

$$\mathrm{H}(x) = \max_{Y} \sum_{i=1}^{k} I(h_i(x) = Y) \tag{4}$$

where $\mathrm{H}(x)$ is the RFC model, $h_i(x)$ is a single decision tree, X is the input vector, Y is the target vector (or classification target), and $I(\cdot)$ is the indicator function.

4.2. Asphalt Pavement Distress Classification

4.2.1. Classification System

According to the classification criterion described in the *Technical Specifications for Maintenance of Highway Asphalt Pavement* [38] and the classification feasibility with the acquired point cloud with an interval of 5 cm, the classification system established in this study focuses on extracting severe pavement distresses (Table 3). On the one hand, the data quality in this research does not allow for the extraction of slight pavement distresses. On the other hand, severe distress is indicative of the fact that the pavement has entered into the latter phase of aging. Once this type of distress appears, the pavement has lost its normal function as a platform for vehicles to drive on and it needs urgent maintenance. Therefore, we established a classification system mainly for severe pavement distresses. Because of the similarity between subsidence, rutting, and cracks, they are regarded as the same type of distress in the classification.

Table 3. Classification of typical asphalt pavement distress.

Types of Distress	Grade	Description	Indicator
Potholes	Slight	Shallow hole, small area (<0.1 m^2)	depth $\leq$ 15 mm
	Severe	Deep hole, large area (>0.1 m^2)	depth > 15 mm
Subsidence	Slight	Small deformation	depth $\leq$ 15 mm
	Severe	Large deformation	depth > 15 mm
Rutting	Slight	Shallow, no obvious discomfort in driving	depth $\leq$ 15 mm
	Severe	Deep, clearly bumpy in driving	depth > 15 mm
Cracks	Slight	Fewer branches	width $\leq$ 5 cm
	Severe	More branches	width > 5 cm

4.2.2. Implementation and Results of RFC

In Section 3, a total of 48 features were extracted, including point cloud elevation, reflection intensity, a multiscale roughness index, a multiscale Gaussian curvature, and several object-oriented geometric features. The multiple features of the dataset are listed in Table 4.

Table 4. The multiple features of the dataset.

Feature Category	Feature Description	Measurement Scale	Number of Features
Attributes of the Original Point Cloud	Elevation Reflection intensity		2
Statistical Features of Elevation	Roughness index	Microscopic scale	16
		Macroscopic scale	3
	Gaussian curvature	Microscopic scale	16
		Macroscopic scale	3
Geometric Features	Regional features		4
	Shape features		4

According to the classification system proposed in 4.2.1, RFC was adopted to classify the acquired multiscale and multidimensional dataset. The training samples are reported in Table 5.

RETRACTED

Table 5. Training samples.

Category	Color	Number of Pixels	Number of Polygons
Potholes	Red	951	39
Subsidence	Green	2001	22
Undamaged pavement	Blue	4736	25

During the classification process, we used the cross-validation method to classify the training samples (Figure 16). The training samples were randomly sampled according to a ratio of 4:1, in which 80% of the training data were used for the classification model training and the remaining 20% were used as the validation set for accuracy validation. The cross-validation method can not only validate the classification accuracy, but also demonstrate the stability of the classification method. A total of five experiments were conducted in the classification process. The RFC model that was used during the experiments contained 200 decision trees, and each of these trees had nine features and a maximum tree height of 10. The RFC only used a subset of features to build each individual decision tree. This is advantageous because each decision tree can make a more accurate classification decision based only on effective features, reducing the error that is associated with the structural risk of including the entire feature vector in the analysis. Simply put, each decision tree is a classification "specialist" of the feature domain that is used in it. For a feature used to differentiate a class type, a nonspecialist decision tree adopts a nearly random way of voting, in which the number of the specialist decision trees is sufficient to make an accurate classification when all the decision trees meet a certain number. The training accuracy and testing accuracy are shown in Table 6.

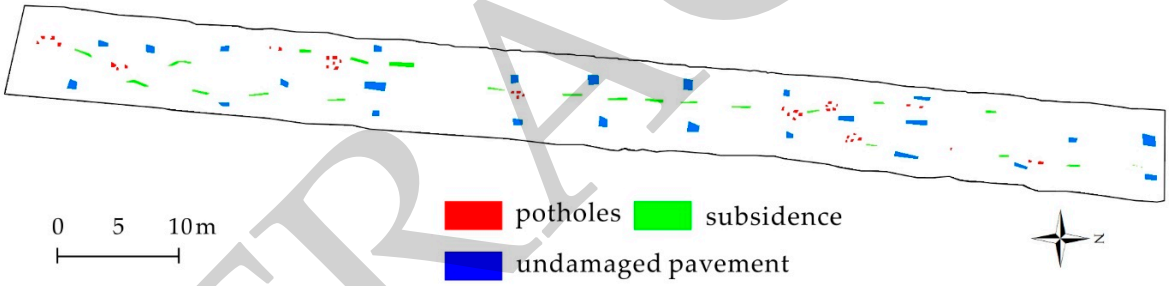


Figure 16. Distribution of the training samples.

Table 6. Statistics of classification accuracy.

Number of Experiments	Training Accuracy (%)			Testing Accuracy (%)		
	Potholes	Subsidence	Undamaged Pavement	Potholes	Subsidence	Undamaged Pavement
1	98.21	98.75	100	95.35	97.53	98.62
2	99.12	100	100	96.56	98.71	98.89
3	97.47	98.43	100	95.86	95.34	98.30
4	99.95	98.56	100	94.10	95.79	98.55
5	98.88	99.20	100	93.32	94.27	98.71

The experimental results show that the method has high classification accuracy and that the accuracy is stable. The aforementioned results not only reflect the validity of the pavement distress extraction model but also indicate the applicability and robustness of the RFC method. In addition, the method has a high training accuracy, while the testing accuracy does not show a significant decline, which indicates a strong robustness to overfitting.

RETRACTED

4.2.3. Accuracy Assessment

To further verify the classification accuracy, we analyzed the classification results with the visual interpretation results as a reference (Table 7).

Table 7. Accuracy assessment with the visual interpretation results as a reference.

Category	Commission Error (%)	Omission Error (%)	Producer's Accuracy (%)	User's Accuracy (%)
Potholes	15.72	20.12	79.88	84.28
Subsidence	31.07	12.47	87.53	68.93
Undamaged pavement	1.52	6.07	93.93	98.48
Overall Accuracy: 92.30%; Kappa Coefficient: 0.9023				

According to Table 7, the overall accuracy is 92.3%. The classification accuracy decreased relative to the cross-validation but it remained greater than 90%. The main classification error of pothole distress originated from omission error, that is, some of the potholes were misclassified as subsidence. When comparing the classification results with the visual interpretation results, it is apparent that some potholes were misclassified as subsidence. The misclassified regions were mainly at the edge of potholes, which is a transitional area of damaged pavement and undamaged pavement (Figure 17c). In these regions, the roughness index and Gaussian curvature were influenced by the surrounding undamaged pavement, and the eigenvalues were not obvious, which resulted in a certain degree of misclassification. In addition to the classification errors in the transitional area, the classification accuracy in the other regions was very high, and the distress distribution could be accurately extracted, which provides a reference for highway maintenance agencies to evaluate road conditions and perform further maintenance.

4.3. Comparison of Different Classification Methods

In this section, we compare the classification results of RFC with maximum likelihood classification (MLC) and support vector machine (SVM) to illustrate that our choice of RFC as the classification method is reasonable. We used the same multifeature dataset and training samples in MLC, and model training was conducted using the cross-validation method for a total of five times. The average training accuracy and testing accuracy were 95.31% and 86.13%, respectively. We selected the classification model with the highest accuracy to extract pavement distresses. The classification result is shown in Figure 17a. The result shows that the commission error of potholes was very serious and a large number of subsidence distresses were misclassified as potholes. This is because the MLC method did not effectively utilize multiscale elevational features and neighborhood statistical features. The same dataset and training samples were used in SVM. We chose a radial basis function as the kernel function, and the penalty factor was 100. The model was trained five times, and the average training accuracy and testing accuracy was 98.95% and 94.83%, respectively. The classification model with the highest accuracy was selected to extract pavement distress, and the result is shown in Figure 17b. As Figure 17b shows, the visual effect of the classification result obtained by SVM was greatly improved when compared with that of MLC. SVM was superior to the MLC method in addressing high-dimensional data, and the testing accuracy was improved from 86.13% to 94.83%. However, it was found that the two types of pavement distress were relatively large in the SVM classification and that undamaged pavement within a certain range of the distress was also misclassified as potholes or subsidence. Because of the correlations between the multiscale roughness index and Gaussian curvature, the multidimensional features restricted one another when a superplane was established in the multidimensional space, which limited the expression of the object-oriented features and resulted in commission errors at the edge of the pavement distress.

RETRACTED

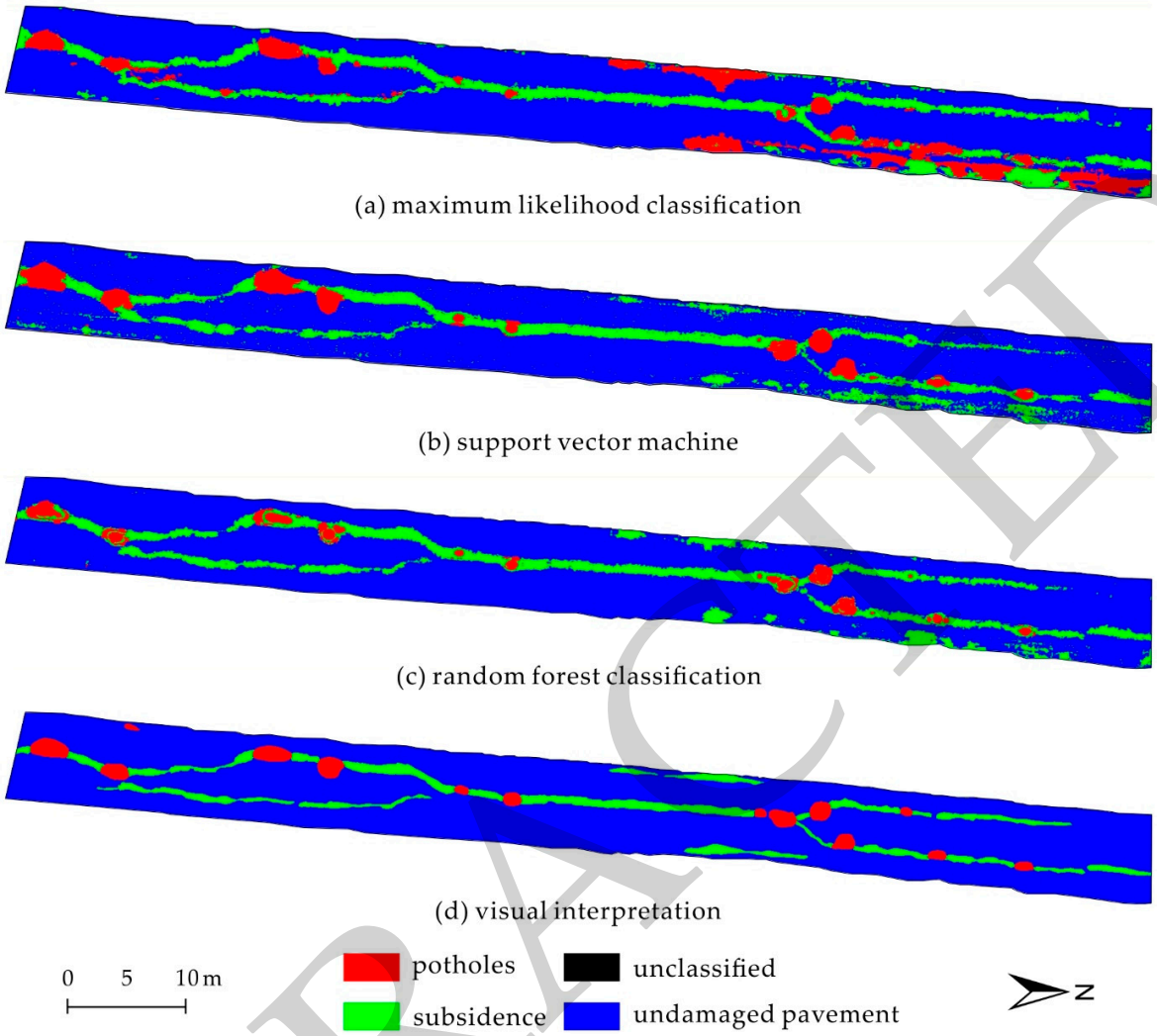


Figure 17. Results of several classification methods.

The classification results that were obtained with MLC and SVM were compared with the results of RFC (Figure 17). Simultaneously, the artificial visual interpretation results were used to verify the classification results. A comparison of the different methods is shown in Table 8.

Table 8. Comparison of different methods.

Classification Method	MLC (%)	SVM (%)	RFC (%)
Overall Accuracy	79.35%	87.88%	92.30
Kappa Coefficient	0.7762	0.8651	0.9023

The comparative results show that the RFC classification stood out with the highest classification accuracy (Table 8), indicating its effectiveness in handling high-dimensional data classification. The difference between the simulation accuracy and the actual validation accuracy of the RF classification is approximately 5% smaller than that of MLC and SVM. This means that the RF classification has the stronger generalization capacity in the training process, while the other two tend to over fit their model to the training data. This has further proved that the RFC's strategy of decision making based on the combined voting outperformed the MLC and SVM classifiers. A part of the decision trees in the classification model can effectively employ object-oriented features to determine the exact boundary of pavement distress, while the other part of the decision trees can vote for the specific type of distress with spectral features and multiscale elevational features. Therefore, the RFC

RETRACTED

method obtained the most reasonable classification result in asphalt pavement distress classification and the overall accuracy of this method was also the highest.

4.4. Application and Validation

In this section, we applied the method proposed in this paper to the validation data to verify its stability. The acquisition and preprocessing of the validation data were the same as the experimental data. A multifeature dataset that included 48 features was extracted according to the elevation and reflection intensity of the original point cloud. The RFC method was adopted to conduct pavement distress classification. The classification results are shown in Figure 18.

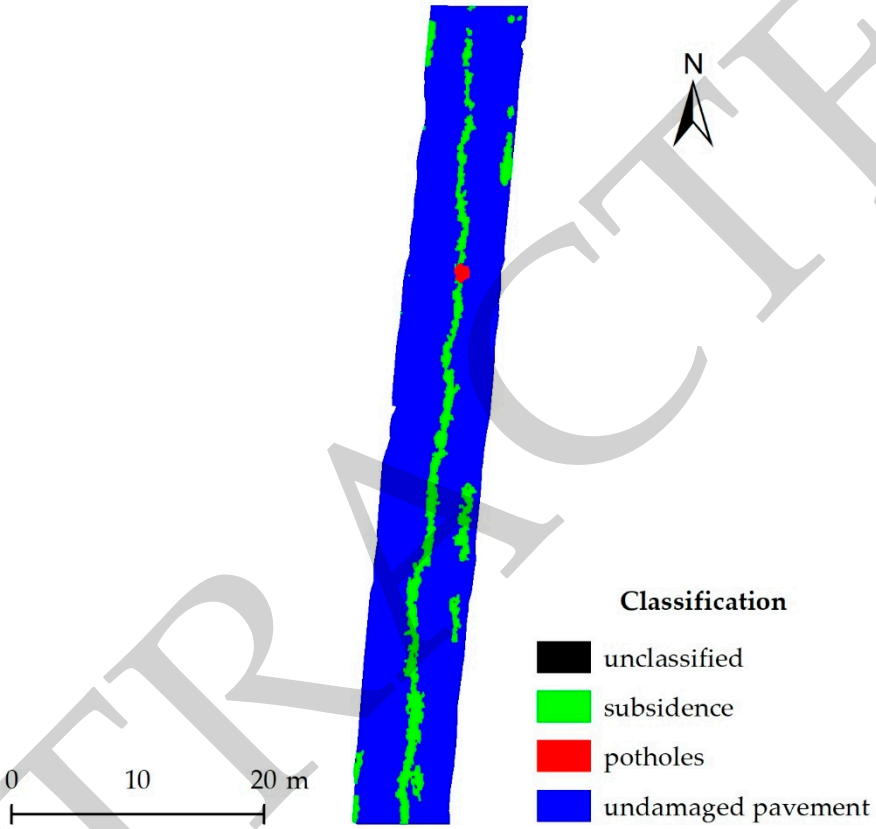


Figure 18. Pavement distress classification results of the validation data.

We utilized independent testing samples to verify the accuracy of the classification results, which is shown in Table 9.

Table 9. Classification accuracy of the validation data.

Category	Commission Error (%)	Omission Error (%)	Producer's Accuracy (%)	User's Accuracy (%)
Potholes	1.59	0.32	99.68	98.41
Subsidence	8.10	5.76	94.24	91.90
Undamaged pavement	2.13	7.41	92.59	97.87
Overall Accuracy: 95.86%; Kappa Coefficient: 0.9389				

According to the classification results and the accuracy validation table, the pavement distress classification method achieved a high accuracy when it was applied to the validation data. The overall

RETRACTED

accuracy was 95.86% and the Kappa coefficient was 0.9389. The classification accuracy of potholes was nearly 99%, while there was a certain degree of commission error in extracting subsidence distress. Combined with the reflection intensity image of the validation data, the damaged regions at the edge of subsidence areas were misclassified as subsidence distress. In these regions, the roughness index and Gaussian curvature were influenced by the surrounding pavement, and the eigenvalues were not obvious, which resulted in a certain degree of misclassification. However, the overall accuracy of the classification results was still high. Therefore, by using distress classification and the results analysis of the validation data, it is evident that our method was reliable and stable.

5. Conclusions

This research has demonstrated the application of random forest classification in identifying pavement distress, based on the use of UAV LiDAR point cloud data. To address the difficulties in distress classification using the conventional method, an effective set of features were found, including the spectral and spatial ones that could be derived from the LiDAR point cloud. A case study was conducted to classify the pavement distress in North Xinjiang, China based on the analysis of the elevations and intensities of the point cloud data. The random forest classification model was successfully developed with 48 features (e.g., elevation, intensity, roughness, curvature, geometric), and a satisfactory classification with an accuracy of 92.3% was achieved. It was found that the overall accuracy of the RFC was 5–10% greater than that of the MLC and SVM classifiers. The incorporation of spectral, elevation, and geometrical features extracted from the UAV LiDAR point cloud into the random forest classification can produce better a delineation of the potholes and subsidence from the undamaged pavement. In conclusion, the flexible UAV platform, configured with a laser scanner, provides a valuable tool for monitoring of the asphalt pavement condition.

In future work, more UAV LiDAR point cloud data of different road areas and segments could be used to further evaluate the performance of the method for the identification of potholes and subsidence. Because of the spatial resolution limitation, the UAV LiDAR point cloud that was used in this paper still cannot detect slight distress. Therefore, higher resolution point cloud should be obtained to further increase the accuracy of pavement condition evaluation. In addition, other remote sensing data, including multispectral images by UAV, also have a great potential for pavement condition monitoring. A more accurate classification of pavement distress may be achieved through comprehensive analysis of a high-density point cloud and multispectral remote sensing images.

Author Contributions: All five authors contributed to the work presented in this paper. Z.L. and C.C. formed the original idea. Z.L. and S.T. worked on the experiment and data analysis. Z.L., M.-P.K., and X.T. wrote the paper. All authors worked collaboratively on revising the manuscript.

Funding: This research was funded by the National Key Research and Development Program of China, grant number 2017YFB0503700, and the High-Resolution Earth Observation System National Key Foundation of China, grant numbers 11-Y20A02-9001-16/17 and 30-Y20A01-9003-16/17.

Acknowledgments: The support provided by the China Scholarship Council (CSC) is acknowledged. The authors are sincerely grateful for the comments of the anonymous reviewers and members of the editorial team.

Conflicts of Interest: The authors declare no conflicts of interest.

References

1. Rodrigue, J.; Comtois, C.; Slack, B. *The Geography of Transport Systems*, 3rd ed.; Routledge: London, UK, 2013; pp. 1–10, ISBN 9781136777325.
2. Ministry of Transport of the People's Republic of China. Available online: http://zizhan.mot.gov.cn/zfxxgk/bnssj/zhghs/201803/t20180329_3005087.html (accessed on 9 May 2018).
3. Lopes, M.; Zhao, D.; Chailleux, E.; Kane, M.; Gabet, T.; Petiteau, C.; Soares, J. Characterization of ageing processes on the asphalt mixture surface. *Road Mater. Pavement Des.* **2014**, *15*, 477–487. [CrossRef]
4. Herold, M.; Roberts, D. Spectral characteristics of asphalt road aging and deterioration: Implications for remote-sensing applications. *Appl. Opt.* **2005**, *44*, 4327–4334. [CrossRef] [PubMed]

RETRACTED

5. Hartgen, D.T.; Fields, M.G.; Feigenbaum, B. *21st Annual Report on the Performance of State Highway Systems (1984–2012)*; Reason Foundation: Los Angeles, CA, USA, 2014.
6. Bandara, N.; Gunaratne, M. Current and future pavement maintenance prioritization based on rapid visual condition evaluation. *J. Transp. Eng.* **2001**, *127*, 116–123. [CrossRef]
7. Schnebele, E.; Tanyu, B.F.; Cervone, G.; Waters, N. Review of remote sensing methodologies for pavement management and assessment. *Eur. Transp. Res. Rev.* **2015**, *7*, 7. [CrossRef]
8. Shah, Y.U.; Jain, S.S.; Tiwari, D.; Jain, M.K. Development of overall pavement condition index for urban road network. In *Procedia-Social and Behavioral Sciences, Proceedings of the 2nd Conference of Transportation-Research-Group-of-India (CTRG), Agra, India, 12–15 December 2013*; Elsevier: Amsterdam, The Netherlands, 2013; pp. 332–341. [CrossRef]
9. Pulugurtha, S.S.; Ogunro, V.; Pando, M.A.; Patel, K.J.; Bonsu, A. Preliminary results towards developing thresholds for pavement condition maintenance: Safety perspective. In *Procedia-Social and Behavioral Sciences, Proceedings of the 2nd Conference of Transportation-Research-Group-of-India (CTRG), Agra, India, 12–15 December 2013*; Elsevier: Amsterdam, The Netherlands, 2013; pp. 302–311. [CrossRef]
10. Proto, M.; Bavusi, M.; Bernini, R.; Bigagli, L.; Bost, M.; Bourquin, F.; Cottineau, L.M.; Cuomo, V.; Vecchia, P.D.; Dolce, M.; et al. Transport infrastructure surveillance and monitoring by electromagnetic sensing: The ISTIMES project. *Sensors* **2010**, *10*, 10620–10639. [CrossRef] [PubMed]
11. Kim, H.; Soleymani, H.; Han, H.; Nam, H. Evaluation of asphalt pavement crack sealing performance using image processing technique. In Proceedings of the International Symposium on Automation and Robotics in Construction (ISARC), Tokyo, Japan, 3–5 October 2006; pp. 341–345.
12. McGhee, K.H. *Automated Pavement Distress Collection Techniques—A Synthesis of Highway Practice*; National Cooperative Highway Research Program, Transportation Research Board: Washington, DC, USA, 2004.
13. Cheng, H.; Chen, J.; Glazier, C.; Hu, Y. Novel approach to pavement cracking detection based on fuzzy set theory. *J. Comput. Civ. Eng.* **1999**, *13*, 270–280. [CrossRef]
14. Attoh-Okine, N.; Adarkwa, O. *Pavement Condition Surveys—Overview of Current Practices*; Delaware Center for Transportation, University of Delaware: Newark, DE, USA, 2013.
15. Themistocleous, K.; Neocleous, K.; Pilakoutas, K.; Hadjimitsis, D.G. Damage assessment using advanced non-intrusive inspection methods: Integration of space, UAV, GPR, and field spectroscopy. In Proceedings of the 2nd International Conference on Remote Sensing and Geoinformation of the Environment (RSCy), Paphos, Cyprus, 7–10 April 2014; Volume 9229. [CrossRef]
16. Shahi, K.; Shafri, H.Z.; Taherzadeh, E.; Mansor, S.; Muniandy, R. A novel spectral index to automatically extract road networks from WorldView-2 satellite imagery. *Egypt. J. Remote Sens. Space Sci.* **2015**, *18*, 27–33. [CrossRef]
17. Wang, C.; Hu, Q.; Lu, Q. Research on a novel low modulus OFBG strain sensor for pavement monitoring. *Sensors* **2012**, *12*, 10001–10013. [CrossRef]
18. Skoglar, P.; Orguner, U.; Tornqvist, D.; Gustafsson, F. Road target search and tracking with gimballed vision sensor on an unmanned aerial vehicle. *Remote Sens.* **2012**, *4*, 2076–2111. [CrossRef]
19. Mohammadi, M. Road classification and condition determination using hyperspectral imagery. In *International Archives of the Photogrammetry Remote Sensing and Spatial Information Sciences, Proceedings of the 22nd Congress of the International-Society-for-Photogrammetry-and-Remote-Sensing, Melbourne, Australia, 25 August–1 September 2012*; Copernicus Publications: Göttingen, Germany, 2012; pp. 141–146.
20. Italos, C.; Hadjimitsis, D.G.; Alexakis, D.D.; Themistocleous, K.; Agapiou, A.; Nisantzi, A.; Papoutsa, C.; Papadavid, G. Integrated Use of Satellite Remote Sensing and GIS for the Development of a Sophisticated Sustainability Index for Urban Areas: A Case Study of Paphos City (Cyprus). In Proceedings of the 32nd EARSeL Symposium Advances in Geosciences, Mykonos Island, Greece, 21–24 May 2012; Volume 2124, pp. 587–593.
21. Alessandro, M.; Nicola, F.; Rosamaria, S.; Antonio, D.; Maurizio, F. Spectroradiometric Laboratory Measures on Asphalt Concrete: Preliminary Results. In *Procedia-Social and Behavioral Sciences, Proceedings of the 5th International Congress on Sustainability of Road Infrastructures (SIIV), Rome, Italy, 29–31 October 2012*; D'Andrea, A., Moretti, L., Eds.; Elsevier: Amsterdam, The Netherlands, 2012; pp. 514–523. [CrossRef]
22. Marcondes, J.; Burgess, G.J.; Harichandran, R.; Snyder, M.B. Spectral-Analysis of Highway Pavement Roughness. *J. Transp. Eng.* **1991**, *117*, 540–549. [CrossRef]

RETRACTED

23. Mei, A.; Salvatori, R.; Fiore, N.; Allegrini, A.; D'Andrea, A. Integration of field and laboratory spectral data with multi-resolution remote sensed imagery for asphalt surface differentiation. *Remote Sens.* **2014**, *6*, 2765–2781. [CrossRef]
24. Moropoulou, A.; Avdelidis, N.P.; Koui, M.; Kakaras, K. An application of thermography for detection of delaminations in airport pavements. *NDT E Int.* **2001**, *34*, 329–335. [CrossRef]
25. Pan, Y.; Zhang, X.; Tian, J.; Jin, X.; Luo, L.; Yang, K. Mapping asphalt pavement aging and condition using multiple endmember spectral mixture analysis in Beijing, China. *J. Appl. Remote Sens.* **2017**, *11*, 016003. [CrossRef]
26. Zhang, C.; Elaksher, A. An unmanned aerial vehicle-based imaging system for 3D measurement of unpaved road surface distresses. *Comput.-Aided Civ. Infrastruct. Eng.* **2012**, *27*, 118–129. [CrossRef]
27. Paska, E.P. State-of-the-Art Remote Sensing Geospatial Technologies in Support of Transportation Monitoring and Management. Ph.D. Thesis, The Ohio State University, Columbus, OH, USA, 2009.
28. Tsai, Y.; Jiang, C.; Wang, Z. Pavement crack detection using high-resolution 3D line laser imaging technology. In *7th RILEM International Conference on Cracking in Pavements*; Scarpas, A., Kringos, N., Al-Qadi, I.A.L., Eds.; RILEM Bookseries; Springer: Dordrecht, The Netherlands, 2012; Volume 4.
29. Li, Q.; Yao, M.; Yao, X.; Xu, B. A real-time 3D scanning system for pavement distortion inspection. *Meas. Sci. Technol.* **2010**, *21*, 015702. [CrossRef]
30. Chang, K.; Chang, J.; Liu, J. Detection of pavement distresses using 3D laser scanning technology. In Proceedings of the International Conference on Computing in Civil Engineering, Cancun, Mexico, 12–15 July 2005.
31. Puri, A. *A Survey of Unmanned Aerial Vehicles (UAV) for Traffic Surveillance*; Technical Paper; Department of Computer Science and Engineering, University of South Florida: Tampa, FL, USA, 2005; pp. 1–29.
32. Kim, H.; Sim, S.H.; Cho, S.; Nam, H. Unmanned aerial vehicle (UAV)-powered concrete crack detection based on digital image processing. In Proceedings of the 6th International Conference on Advances in Experimental Structural Engineering, 11th International Workshop on Advanced Smart Materials and Smart Structures Technology, Champaign, IL, USA, 1–2 August 2015.
33. Ersoz, A.B.; Pekcan, O.; Teke, T. Crack identification for rigid pavements using unmanned aerial vehicles. *IOP Conf. Ser. Mater. Sci. Eng.* **2017**, *236*, 012101. [CrossRef]
34. Hoang, N.D.; Nguyen, Q.L.; Bui, D.T. Image Processing–Based Classification of Asphalt Pavement Cracks Using Support Vector Machine Optimized by Artificial Bee Colon. *J. Comput. Civ. Eng.* **2018**, *32*, 04018037. [CrossRef]
35. Pan, Y.; Zhang, X.; Cervone, G.; Yang, L. Detection of Asphalt Pavement Potholes and Cracks Based on the Unmanned Aerial Vehicle Multispectral Imagery. *IEEE J. Sel. Top. Appl. Earth Obs. Remote Sens.* **2018**, *11*, 3701–3712. [CrossRef]
36. Georgopoulos, A.; Loizos, A.; Flouda, A. Digital image processing as a tool for pavement distress evaluation. *ISPRS J. Photogramm. Remote Sens.* **1995**, *50*, 23–33. [CrossRef]
37. Eskin, E. Anomaly detection over noisy data using learned probability distributions. In Proceedings of the International Conference on Machine Learning, San Francisco, CA, USA, 29 June–2 July 2000.
38. Ministry of Transport of the People's Republic of China. *Industrial standards of the People's Republic of China: Technical Specifications for Maintenance of Highway Asphalt Pavement*; China Communications Press: Beijing, China, 2001; pp. 10–12, ISBN 978151140551.
39. Cavalli, M.; Tarolli, P.; Marchi, L.; Fontana, G.D. The effectiveness of airborne LiDAR data in the recognition of channel-bed morphology. *Catena* **2008**, *73*, 249–260. [CrossRef]
40. Vianello, A.; Cavalli, M.; Tarolli, P. LiDAR-derived slopes for headwater channel network analysis. *Catena* **2009**, *76*, 97–106. [CrossRef]
41. Gauss, K.F. *General Investigations of Curved Surfaces: Edited with an Introduction and Notes by Peter Pesic*; Courier Corporation: North Chelmsford, MA, USA, 2013; pp. 79–110, ISBN 9780486154817.
42. Huang, X.; Li, N.; Zhang, F.; Wan, W. Automatic power lines extraction method from airborne lidar point cloud. *Geomat. Inf. Sci. Wuhan Univ.* **2015**, *40*, 1563–1569. [CrossRef]
43. Rodriguez-Galiano, V.F.; Ghimire, B.; Rogan, J.; Chica-Olmo, M.; Rigol-Sanchez, J.P. An assessment of the effectiveness of a random forest classifier for land-cover classification. *ISPRS J. Photogramm. Remote Sens.* **2012**, *67*, 93–104. [CrossRef]

RETRACTED

44. Fang, K.; Wu, J.; Zhu, J.; Shi, B. A review of technologies on random forests. *Stat. Inf. Forum* **2011**, *26*, 32–38.
45. Breiman, L. Random forests. *Mach. Learn.* **2001**, *45*, 5–32. [CrossRef]



© 2019 by the authors. Licensee MDPI, Basel, Switzerland. This article is an open access article distributed under the terms and conditions of the Creative Commons Attribution (CC BY) license (http://creativecommons.org/licenses/by/4.0/).

RETRACTED